# Width and Sidewall Effects on High Speed Cavity Flows

Yiyang Sun[*] Yang Zhang[†] Kunihiko Taira[‡] Louis N. Cattafesta III[§]
*Florida State University, Tallahassee, FL*

Benjamin George[¶] and Lawrence S. Ukeiley[‖]
*University of Florida, Gainesville, FL*

**The present work examines the influence of cavity width, sidewall boundary conditions, free stream Mach numbers, and Reynolds numbers on open rectangular cavity flows. Three-dimensional direct numerical simulations and large eddy simulations are performed for open-cavity flows with length-to-depth ratio $L/D = 6$, width-to-depth ratio $W/D = 1$ and 2 for Reynolds number of $Re_D = 500$ and $10^4$. To numerically examine the effects of sidewall on the flows, we consider (1) two-dimensional cavities with spanwise periodicity and (2) finite-span cavities with no-slip adiabatic walls. Furthermore, the analyses are conducted for subsonic ($M_\infty = 0.6$) and supersonic ($M_\infty = 1.4$) speeds to reveal compressibility effect on the base flow. Companion experiments are carried out for sidewall-to-sidewall and finite-span cavities in the subsonic and supersonic wind tunnels at similar operating conditions but with $Re_D \sim 10^5$. We find that at low $Re_D$, widening the cavity can decrease the velocity fluctuations of the flow by introducing spanwise variations in the flow fields. For turbulent flows at $M_\infty = 0.6$ and 1.4, the spanwise variations in the flow fields are also captured, but the influence of cavity width on velocity fluctuations is moderate, as the dominant spanwise fluctuations are triggered from turbulent mixing. However, streamwise velocity fluctuations decrease in the finite-span cavity compared to the cavity with spanwise periodic boundary condition.**

## I. Introduction

Flows over open cavities are affected by various parameters, which includes geometry, hydrodynamic and acoustic characteristics of the incoming flow.[1] A shear layer emanates from the leading edge of cavity and is naturally unstable. This unstable flow amplifies perturbations as the flow convects downstream. The amplified perturbations create large vortical structures that impinge on the aft wall of the cavity creating intense pressure fluctuations. The generated pressure fluctuations propagate upstream inducing new perturbations at the leading edge, which forms a feedback process and makes the resulting oscillations self-sustained.[1,2]

The oscillations associated with open-cavity flows are generally not desirable as they may lead to damage of cavity structures due to intense pressure fluctuations. In aerospace applications, flows over landing gear wells and weapon bays share similar features with open-cavity flows. During the past few decades, researchers

[*]Graduate Research Assistant, Department of Mechanical Engineering and Florida Center for Advanced Aero-Propulsion, ys12d@my.fsu.edu.

[†]Graduate Research Assistant, Department of Mechanical Engineering and Florida Center for Advanced Aero-Propulsion, yz12b@my.fsu.edu.

[‡]Assistant Professor, Department of Mechanical Engineering and Florida Center for Advanced Aero-Propulsion, ktaira@fsu.edu.

[§]Eminent Scholar and Professor, Department of Mechanical Engineering and Florida Center for Advanced Aero-Propulsion, lcattafesta@fsu.edu.

[¶]Graduate Research Assistant, Department of Mechanical and Aerospace Engineering and Florida Center for Advanced Aero-Propulsion, b.george@ufl.edu.

[‖]Associate Professor, Department of Mechanical and Aerospace Engineering and Florida Center for Advanced Aero-Propulsion, ukeiley@ufl.edu.

have investigated how to suppress the oscillations through various passive and active flow control strategies.[3] However, there have not been clear control guidelines that can be applied to cavity flows in a most general manner. As the baseline of cavity flow changes with different operating Reynolds number, Mach number and cavity geometry, the control approach for suppressing aerodynamic fluctuations has to be tailored for each case. For a wide range of operating conditions, a detailed study will improve our understanding of the baseline uncontrolled flow under specific conditions and help with designing control strategies.

Rectangular cavity flows can be characterized by the non-dimensional parameters of cavity length-to-depth ratio $L/D$, cavity width-to-depth ratio $W/D$, boundary layer thickness at the leading edge $L/\theta_0$, Mach number, and Reynolds number, in addition to the sidewall conditions.[1,4–6] Our previous work[7] studies the effects of Mach number and Reynolds numbers on cavity flows via two-dimensional simulations. In three-dimensional cavity flows, the spanwise boundary conditions are implemented in different manners in experiments and simulations, which can affect the flow characteristics as well. In an experimental setup, a full-span cavity is modeled by extending the span of the test cavity to the full width of a wind tunnel test section. The effects of sidewall and width of cavity are usually neglected by examining the flow field only in the center region. In simulations, spanwise periodic boundary conditions are prescribed. Wavelengths of spanwise flow structures that can be captured in the simulations are constrained by the spanwise computational domain size.

It has been noticed that sidewalls of a finite-span cavity can affect the dominant oscillation mechanism of open-cavity flows. Beresh et al.[6] examined flows over cavities with length-to-width ratios $L/W = 1.00$, 1.67 and 5.00 to uncover the finite-span effects on flow characteristics. They found that the recirculation region inside the cavity and the turbulent intensity are functions of the length-to-width ratio of the finite-span cavity. A combination of experiments and numerical simulations were conducted by Arunajatesan et al.[5] to examine the variation of dominant modes due to different length-to-width ratios. They found that there are strong shear layer oscillations and pressure fluctuations within a wide cavity. It was also noted that the effect of sidewall vortices are observable in a narrow cavity.

To further understand the 3D instabilities of cavity flow affected by spanwise conditions, global stability analysis techniques are used to identify the characteristics of 3D modes in the cavity flows. Brès and Colonius[8] and Vicente et al.[9] performed global instability analysis on low-Reynolds-number cavity flows to identify spanwise instabilities. They found that the most unstable three-dimensional modes have an order-of-magnitude lower frequency than those of the resonant modes in the cavity.

In past studies, only a few three-dimensional numerical simulations were performed for a long cavity with $L/D = 6$ to examine the spanwise effects on flow fields. Most of the simulations[1] on turbulent cavity flows were using URANS which cannot well-resolve the unsteadiness of flows, and the shocks in supersonic flows are rarely discussed. Therefore, the objective of this study is to characterize the spanwise effects in open-cavity flows at subsonic ($M_\infty = 0.6$) and supersonic ($M_\infty = 1.4$) conditions using DNS and LES for laminar ($Re_D = 500$) and turbulent ($Re_D = 10^4$) flows, respectively. The spanwise effects from cavity width and sidewalls in finite-span cavity on flow fields are examined numerically. Shocks and compression waves are also captured with the LES results at supersonic condition. Companion experiments are conducted at $Re_D \sim 10^5$ at both subsonic and supersonic conditions to examine the flow mechanism. In Section II, the numerical simulation approach and experimental setup are presented. Discussion on flow physics regarding flow conditions and spanwise boundary conditions are offered in Section III.

## II. Analysis Setups

### A. Computational Setup

Three-dimensional direct numerical simulations (DNS) and large eddy simulations (LES) have been performed for flows over cavity with $L/D = 6$ using high-fidelity compressible flow solver *CharLES*.[10] The solver uses a finite volume method to numerically solve the Navier-Stokes equations on structured or unstructured grids. The Vreman model[11] is implemented as a subgrid-scale model to perform large-eddy-simulations for turbulent flow. Harten-Lax-van Leer contact (HLLC)[12] scheme is used to capture the shocks formed in supersonic flow. The present simulation effort builds upon our previous work of two-dimensional analysis[7] of laminar flow over rectangular cavities over the Mach number range from 0.2 to 1.6. In the full-span cavity cases, the present computation extends the two-dimensional setup with spanwise periodic boundary conditions prescribed. The width-to-depth ratios of the domain are $W/D = 1$ and 2 for cavity flows at $Re_D = 500$ using DNS and $Re_D = 10^4$ using LES in the present investigation. For the cases of finite-span

cavity, walls are added parallel to the streamwise directions with no-slip and adiabatic boundary conditions. The width of the finite-span cavity is $W/D = 2$ and the incoming flows are prescribed with $M_\infty = 0.6$ and 1.4 at $Re_D = 10^4$. Detailed information about the simulation setups and conditions are shown in Table 1 and Figure 1. Perturbations are added at the inlet velocity profile to model an incoming turbulent boundary layer by superposing random Fourier modes.[13,14] The top and outlet regions of the computational domain are specified as sponge zones to damp out hydrodynamic and acoustic disturbances.[15] The flows are resolved on structured mesh containing 7 million and 14 million grid points of the cavity cases $W/D = 1$ and 2 with spanwise periodic boundary condition, respectively. In the finite-span cavity, the width-to-depth ratio is $W/D = 2$, and slip boundary condition is applied along the farfield sidewalls. Due to a larger domain, the total number of grid points required to resolve flow over the finite-span cavity is approximately 24 million.

| Case | W/D | $M_\infty$ | $Re_D$ | Side BC | Companion Exp. |
|---|---|---|---|---|---|
| W1M06ReLP | 1 | 0.6 | 500 | Periodic | |
| W1M06ReHP | 1 | 0.6 | 10,000 | Periodic | |
| W2M06ReLP | 2 | 0.6 | 500 | Periodic | |
| W2M06ReHP | 2 | 0.6 | 10,000 | Periodic | FSU |
| W2M14ReHP | 2 | 1.4 | 10,000 | Periodic | UF |
| W2M06ReHF | 2 | 0.6 | 10,000 | Finite | FSU |
| W2M14ReHF | 2 | 1.4 | 10,000 | Finite | UF |

**Table 1:** List of three-dimensional simulations for cavity of $L/D = 6$ and availability of companion experiments. The nomenclature for example follows: W2M06ReHP: $W/D = 2$, $M_\infty = 0.6$, $Re_D = 10^4$ (H, high) and spanwise periodic boundary condition (P). The finite-span cavity case is labeled with F.

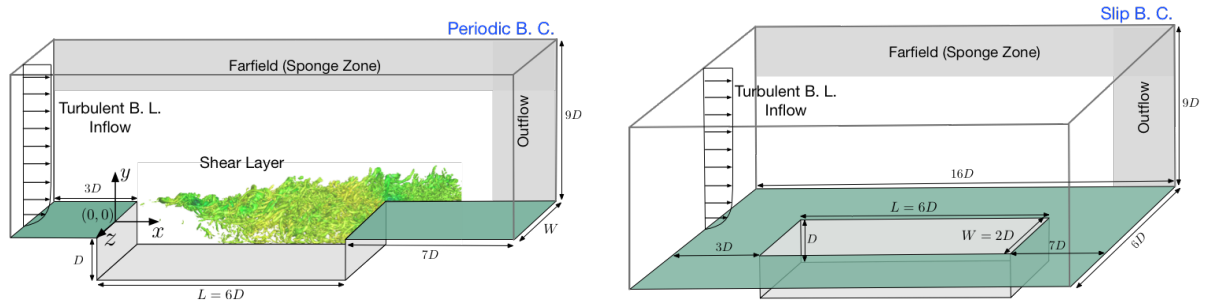


**Figure 1:** Computational setup for cavity flows. (a) Full-span cavity with periodic boundary conditions specified at sidewalls; (b) Finite-span cavity with no-slip boundary conditions applied along the flat plate and inside the cavity, and slip boundary conditions for the farfield sidewall boundaries.

## B. Wind Tunnel Experiment Setups

Companion experiments are conducted at the FSU and UF wind tunnel facilities to study the influences of Mach number and sidewall boundary conditions on the base flows. At the FSU facility, both full-span and finite-span experiments are conducted at $M_\infty = 0.6$ and the schematics of cavity models for subsonic flow are illustrated in Figure 2. At the UF facility, a full-span cavity has been investigated previously,[16] and a finite-span cavity model is examined at $M_\infty = 1.4$ in the current study. All cavity models have a length-to-depth $L/D$ ratio of 6 but the finite-span cavity models have a width-to-depth $W/D$ ratio of 2. Table 2 provides the cavity model dimensions for all the cases.

Non-time resolved particle image velocimetry (PIV) is utilized to measure the mean velocity fields inside all of the cavity models. Similar PIV setups and equipment are employed at both the FSU and UF facilities. All images are acquired and processed using DaVis 8.2 software. At FSU, the velocity along the streamwise plane at the center-span of the full-span cavity is measured using two-component PIV. Stereoscopic PIV is performed along spanwise planes at multiple streamwise locations to measure the instantaneous velocity across the cavity span. Additional details on this PIV setup and the experimental results can be found in the work by Zhang et al.[17] Furthermore, at FSU the finite-span cavity model is tested at $M_\infty = 0.6$ using

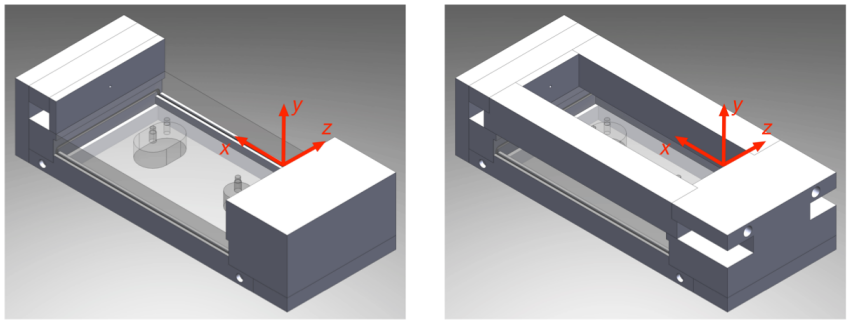


**Figure 2:** Schematic of full- (left) and finite-span (right) cavity models for subsonic cavity flow experiments at FSU.

| | FSU ($M_\infty = 0.6$) | | UF ($M_\infty = 1.4$) | |
|---|---|---|---|---|
| | Full-Span | Finite-Span | Full-Span | Finite-Span |
| Length ($mm$) | 158.8 | 158.8 | 76.2 | 76.2 |
| Width ($mm$) | 101.6 | 52.8 | 76.2 | 25.4 |
| Depth ($mm$) | 26.4 | 26.4 | 12.7 | 12.7 |
| $L/D$ | 6 | 6 | 6 | 6 |
| $W/D$ | 3.85 | 2 | 6 | 2 |

**Table 2:** Cavity model dimensions in experiments at FSU and UF.

two-component PIV but now with two cameras placed adjacent to each other. The cameras are placed at an oblique angle of approximately 17° such that they are peering over the opaque sidewalls into the cavity. This cant angle produces perspective bias errors in the normal velocity component of the PIV images but can accurately measure the streamwise velocity component, as discussed in the work by Beresh et al.[18] In the supersonic cavity flow experiments at UF, stereoscopic PIV is used to measure the three-components of velocity along the streamwise plane at the center-span of the finite-span cavity. Similar to the PIV setup at FSU, the cameras are placed at an oblique angle of approximately 35° to peer over the opaque sidewalls, but in the UF setup the cameras are placed at a stereoscopic half-angle of 12°. Standard stereoscopic PIV calibration methods are conducted to remove the perspective bias error in the normal velocity component measurement. The setup are shown in Figure 3. Additional details of the PIV setup at UF and the experimental results can be found in the work by George et al.[19]

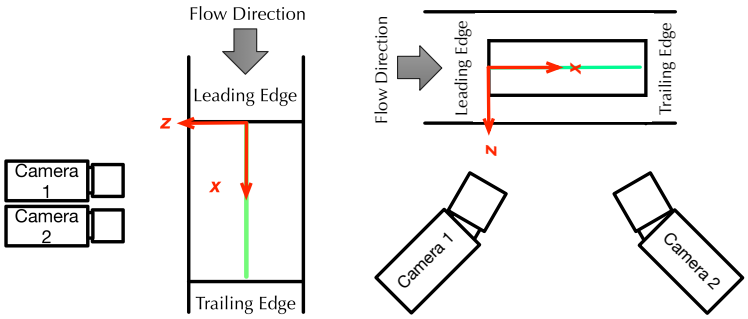


**Figure 3:** Setups of PIV used for investigating the flow fields in cavities. Two-component PIV (left) for full-span cavity and stereoscopic PIV (right) for finite-span cavity.

## III. Results

In this section, we discuss the effects of spanwise boundary condition, Mach number, and Reynolds number on flow features. Instantaneous and time-averaged flow fields are analyzed to reveal the influence from spanwise boundary conditions. Flow fluctuations in each direction are examined to reveal how the spanwise boundary conditions alter the spanwise large-scale turbulent structures. Furthermore, spatial

Fourier transform analysis is performed on the flow field to uncover the spanwise variations characterized by wavelengths.

### A. Instantaneous Flow Field

Some representative instantaneous flow fields for cases W1M06ReHP, W2M06ReHP and W2M06ReHF are presented in Figure 4, which reveal instantaneous flow physics affected by spanwise boundary conditions. $Q$-criterion[20] is utilized to identify the vortex cores in the flow fields. As it can be seen from the side and top views of the cavity flow, the shear layer rolls up into spanwise vortices after the flow passes the leading edge, and convects downstream. The vortex cores correspond to the local pressure minima. In the neighborhood of primary spanwise vortex cores, turbulent vortical structures appear. As these structures advect downstream, the structures break down and lose coherence. The free stream and the inner flows are well mixed by the time the flow reaches the rear part of cavity. In the turbulent cavity flows, an increase of cavity width appears to reduce the spanwise coherence of the vortical structures. The existence of sidewalls in a finite-span cavity further breaks down the spanwise coherence of the vortices in the flow.

Instantaneous flow fields for cases W2M14ReHP and W2M14ReHF are presented in Figure 5 to illustrate the flow features at supersonic condition. From the iso-surface of density gradient $\partial\rho/\partial x$, it can be seen that strong compression waves are formed above the sonic speed surface near the trailing edge of the cavities. The compression waves can also be formed because of the obstructions caused by the large vortex roll-ups in the shear layer. The density gradient above sonic-speed surface is almost two-dimensional in the spanwise periodic case, however, in the finite-span case, the iso-surface is curved due to the spanwise sidewalls. Inside the cavities of both periodic- and finite-span cases, the flow speed is subsonic, and the large density gradients are present from internal turbulence, which have smaller structures compared to the compression waves formed above the sonic-speed iso-surface.

### B. Mean Flow Property

The time-averaged streamlines of centerline plane ($z/D = 0$) for all cases are shown in Figure 6 with background contours representing streamwise velocity $\bar{u}/U_\infty$. The results from two-dimensional simulation in our previous work[7] are also included. At $M_\infty = 0.6$, there are two closed recirculation regions inside the cavity in the two-dimensional simulation at $Re_D = 500$. While the domain is extended in the spanwise direction with $W/D = 1$, the recirculation remains similar to that in 2D flow, which indicates that flow in the cavity with $W/D = 1$ is almost two-dimensional. As the width is increased to $W/D = 2$, there is only one recirculation located inside the cavity. Hence, the mean flow is affected by increasing the spanwise domain to $W/D = 2$ at this low $Re_D$. In the turbulent cases at $Re_D = 10^4$ from LES, the flows with $W/D = 1$ and 2 exhibit two similar recirculation zones, one that is located in the front corner of the cavity and another one that occupies the middle region of the cavity. However, in both periodic- and finite-span cases with $W/D = 2$, a third recirculation zone appears in the rear corner of the cavity. Even though the $Re_D$ in the turbulent simulation is one order less than the full- and finite-span cavity experiments, the time-averaged results from simulations show qualitative agreement for the wall-to-wall setup in experiments. In the simulation of finite-span cavity flow, the two recirculation zones in the center and rear part of cavity are not as prominent as in the cases with spanwise periodic boundary condition. In the related experimental result, it indicates that there is only one recirculation zone inside the cavity.

For the supersonic flow at $M_\infty = 1.4$, two-dimensional laminar flow is stable with one recirculation inside the cavity. When the Reynolds number is higher as shown in the case W2M14ReHP, there are two recirculation zones inside the cavity. In the finite-span cavity case W2M14ReHF, the simulation reveals only one major recirculation zone in the centerline plane. The results from supersonic flow experiments[16] suggest there is one major recirculation inside the cavity, and the recirculation center is near the rear corner of the cavity.

To further examine how the three-dimensional flow features are affected by the spanwise boundaries, oil flow visualizations are performed in the experiments. Fluorescent pigment and oil mixture is applied on the cavity surface, which forms a surface oil flow pattern that fluoresces under UV light. These patterns have some common characteristics: (1) backflow induced by the main recirculation occupies the majority of the floor; (2) two significant vortices roll-ups on the front part of the cavity floor appear. In the full-span cases, the cavity is wide enough that a spanwise-aligned separation line is visible between two vortices. This separation line is located at the place where two recirculation meet in the front region of the cavity floor.

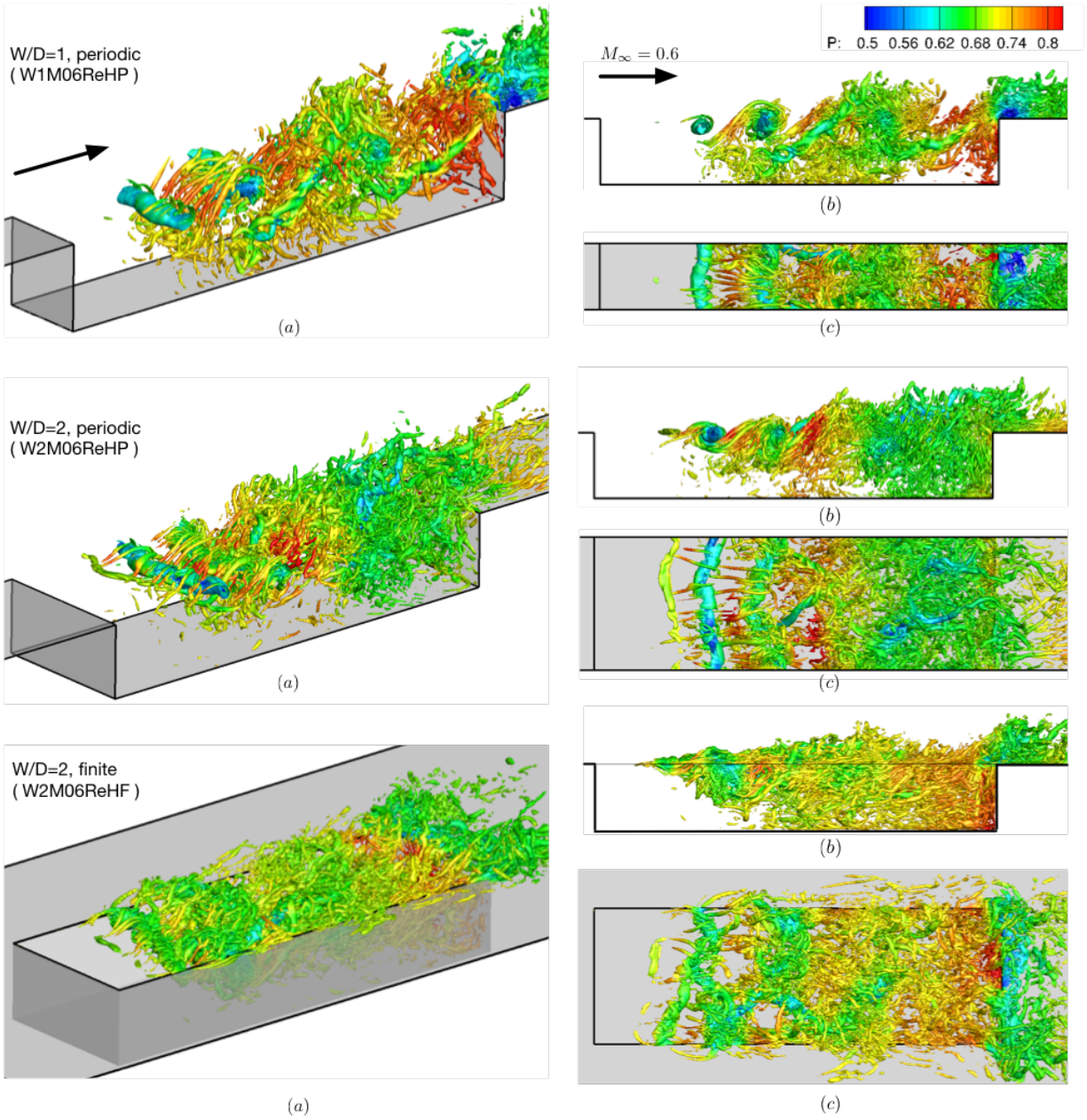


**Figure 4:** Subsonic flows at $M_\infty = 0.6$ over $W/D = 1$ (periodic), $W/D = 2$ (periodic), and $W/D = 2$ (finite) rectangular cavities from simulations. Iso-surfaces of $Q$-criterion ($Q = 5$) are shown with color contours representing pressure for cases W1M06ReHP, W2M06ReHP and W2M06ReHF. Free stream reference pressure is 0.714. (a) Perspective (b) side and (c) top views.

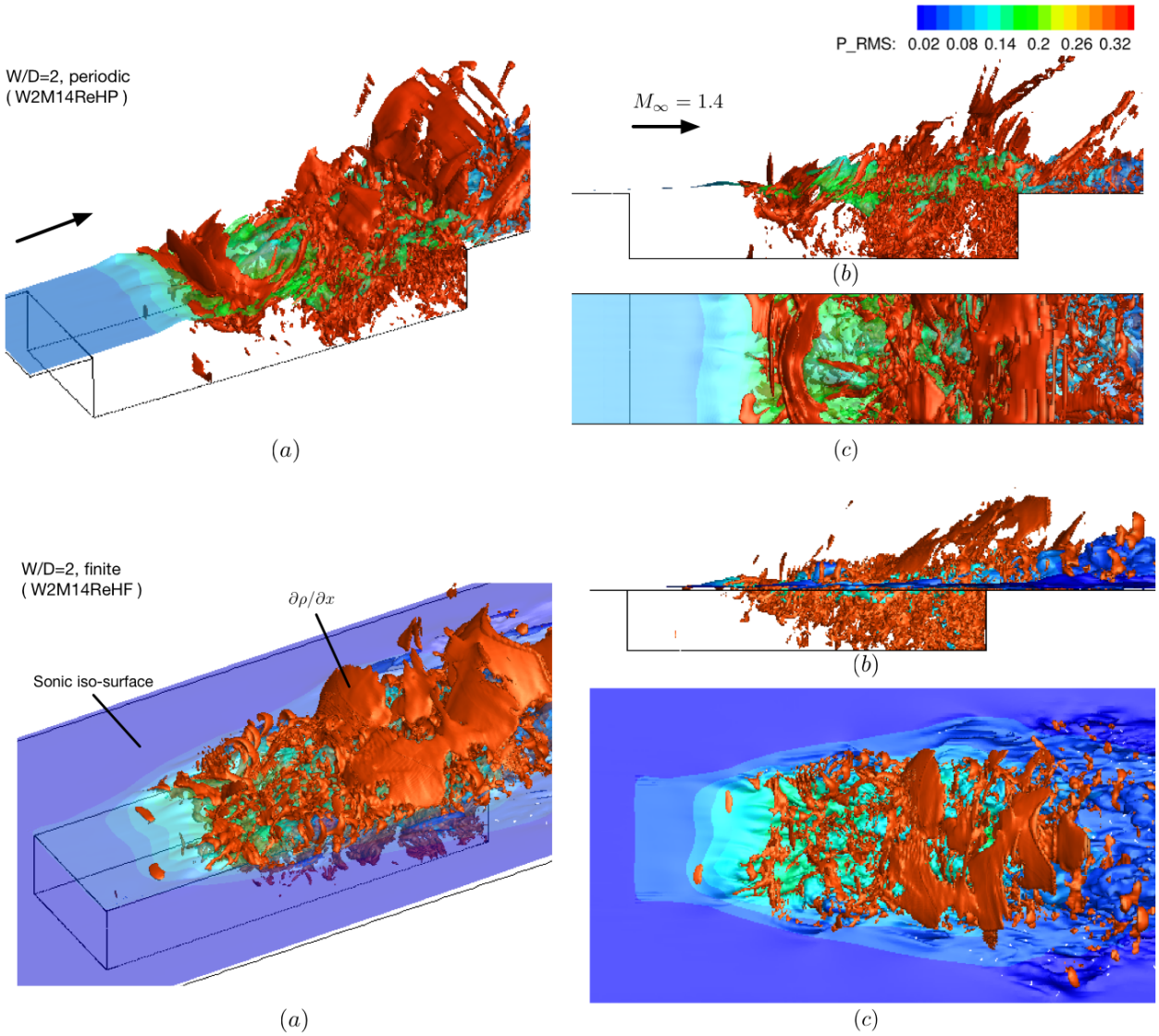


**Figure 5:** Supersonic flows at $M_\infty = 1.4$ are shown over $W/D = 2$ (periodic) and $W/D = 2$ (finite) rectangular cavities from simulations. Iso-surfaces of density gradient ($\partial\rho/\partial x = 0.6$) and sonic-speed surface are presented. The contours of sonic-speed iso-surface represent pressure RMS. Free stream reference pressure is 0.714. (a) Perspective (b) side and (c) top views.

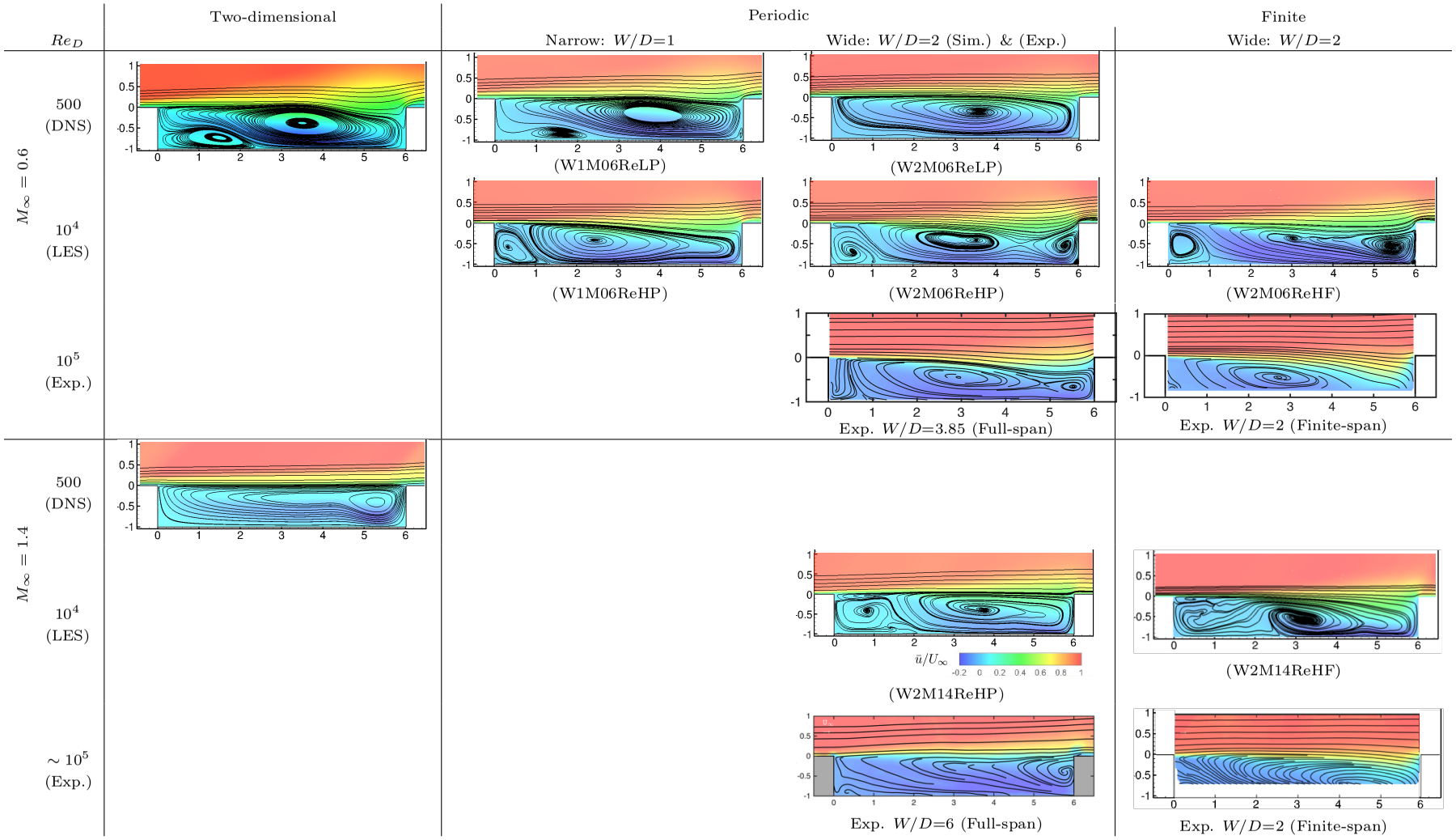


**Figure 6:** Comparison of time-averaged streamlines from centerline slice. The case name is under each plot.

However, when the width is reduced to $W/D = 2$, this separation line is not clearly resolved because the two vortices are close to each other. In Figure 7, the surface oil flow patterns of full-span cases with subsonic flows develop almost only along the streamwise direction in the center region of cavity. The location of separation lines is between $x/D = 0.8$ and 1. Compared to the bottom part of the streamlines in the corresponding simulations in Figure 6, the contacting locations of two recirculation regions near the floor are also around $x/D = 1.0$, which agree with the results from the oil flow visualizations.

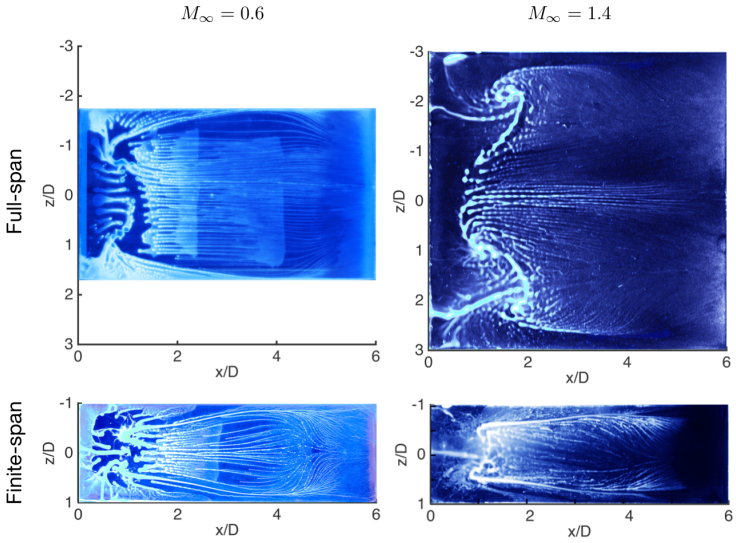


**Figure 7:** Surface oil flow patterns on the cavity floor from experiment.

Next, spreading rate of the shear layer is calculated to characterize the flows at various conditions. Based on the mean flow properties, the vorticity thickness[21] is defined as

$$\delta_\omega = U_\infty / \left( \frac{\partial \bar{u}}{\partial y} \right)_{\max},$$

where $y$ is nondimensionalized by the depth of cavity $D$. It has been noted that the shear layer over the cavity is similar to the free mixing shear layer that there is a linear growth rate when flow detaches the leading edge of the cavity.[22] The major differences between these two types of flows are that cavity flow is in an intense acoustic environment with a feedback process, and the recirculation flow inside the cavity affects the shear layer development.[23] The overall trend of the vorticity thickness development can be seen in Figure 8. The vorticity thickness is averaged in the spanwise direction in the cases with spanwise periodic boundary condition. In the finite-span cases, the vorticity thickness data are extracted from the centerline plane ($z/D = 0$). In the laminar flow cases W1M06ReLP and W2M06ReLP presented in Figure 8 (a), the growth of vorticity thickness is approximately linear. The spreading rate $d\delta_\omega/dx$ is smaller in the case with a wider periodicity ($W/D = 2$). When the flows are turbulent, the spanwise effect on the shear layer spreading rate appears minimal as shown in Figure 8 (b) by the overlap of the vorticity thickness curves. At the supersonic condition (Figure 8 (c)), in the region $x/D \in (0, 3)$, vorticity thickness profiles do not differ much. To assess the difference between the shear layer growth for $x/D \in (3, 6)$, simulation needs to be performed longer to achieve an accurate time-averaged results. The vorticity thickness curves obtained from the centerline plane ($z/D = 0$) in the experiments are compared with the computational results in Figures 8 (d) and (e), which exhibit good agreement. The main difference is that the growth of the vorticity thickness is more linear in the front part of the cavity in the experiments compared to the simulations.

To quantify the spreading rate of shear layer in these cases, data are collected from certain regions listed in Table 3 and are linearly fitted to estimate the growth rate of vorticity thickness. As it can be seen from the growth rates listed in Table 3, as the flow leaves the leading edge ($0 < x/D < 1$), the spreading rate of the shear layer is larger in laminar flow, but as flow convects farther downstream ($1 < x/D < 5$), the spreading rate is increased in the central portion of shear layer in turbulent flows. The comparison between the simulations and experiments shows that the spreading rates of shear layer are close in the center part of cavity ($1 < x/D < 5$) at subsonic condition.

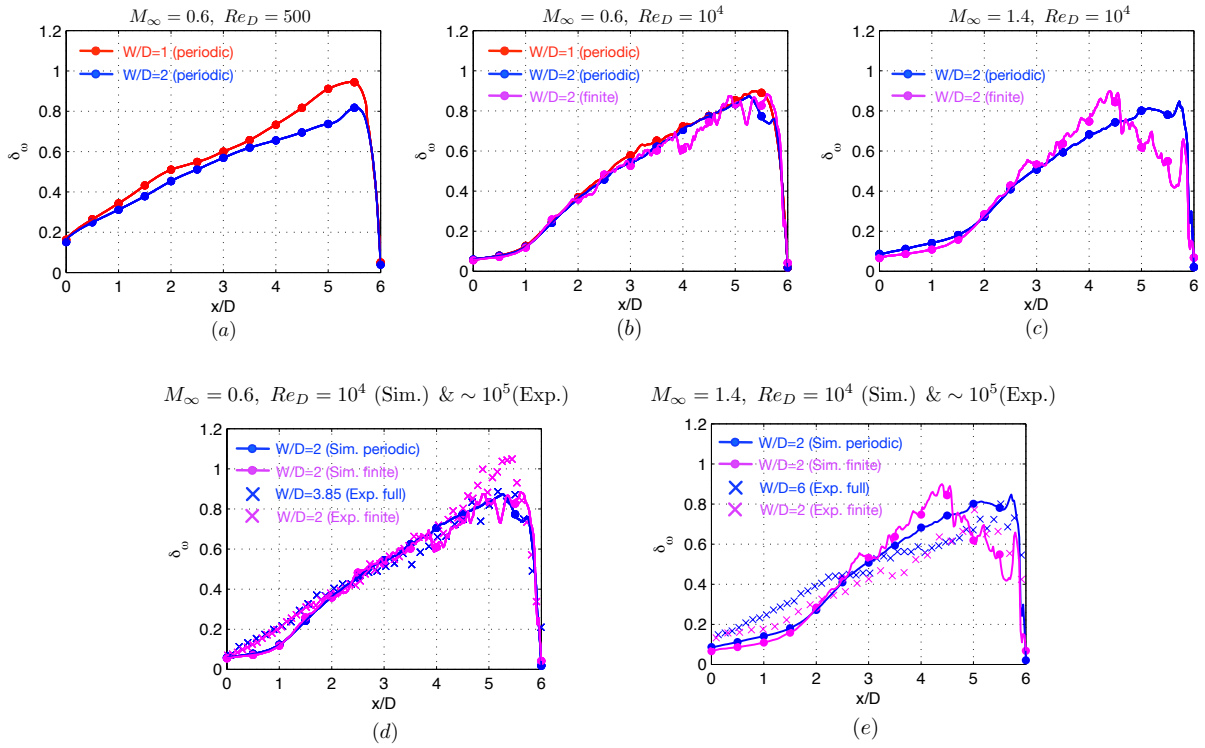


**Figure 8:** Vorticity thickness $\delta_\omega$ obtained from 3D simulations: (a) laminar flow at $M_\infty = 0.6$, (b) turbulent flow at $M_\infty = 0.6$ and (c) turbulent flow at $M_\infty = 1.4$. Comparison between the experiments and the simulations: (d) $M_\infty = 0.6$ and (e) $M_\infty = 1.4$. In the spanwise periodic cases, vorticity thickness is averaged in the spanwise direction; and in the finite-span cases, vorticity thickness is analyzed with data extracted from the centerline plane ($z/D = 0$). All the experimental results are from the centerline plane $z/D = 0$.

| | | $Re_D = 500$ (Sim.) | | $Re_D = 10^4$ (Sim.) | | $Re_D \sim 10^5$ (Exp.) | |
|---|---|---|---|---|---|---|---|
| $M_\infty$ | $W/D$ | $x/D \in (0, 1)$ | (1, 5) | (0, 1) | (1, 5) | (0, 1) | (1, 5) |
| 0.6 | 1 (periodic & full) | 0.1699 | 0.1290 | 0.0598 | 0.1774 | - | - |
| | 2 (periodic & full) | 0.1430 | 0.1060 | 0.0542 | 0.1771 | 0.1205 | 0.1451 |
| | 2 (finite) | - | - | 0.0494 | 0.1668 | 0.1450 | 0.1753 |
| 1.4 | 2 (periodic & full) | - | - | 0.0565 | 0.1812 | 0.1105 | 0.0899 |
| | 2 (finite) | - | - | 0.0380 | - | 0.0442 | 0.0813 |

**Table 3:** Spreading rate of vorticity thickness $d\delta_\omega/dx$.

## C. Fluctuations in Flow Fields

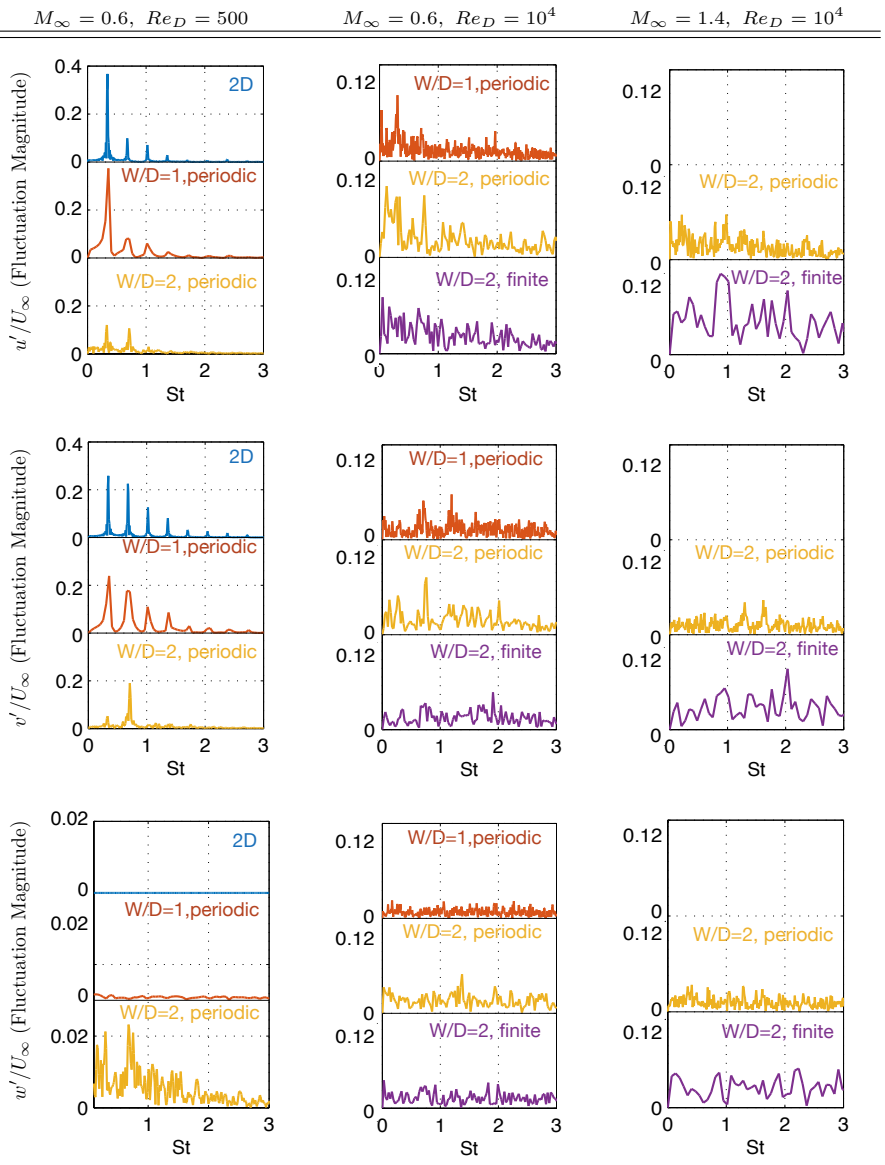


**Figure 9:** Velocity fluctuations along the center plane at location ($x/D = 3,\ y/D = 0$) from simulations. The spectra are shifted vertically and the black lines are reference lines.

A temporal Fourier transform is performed on the local data extracted from the center of the shear layer ($x/D = 3,\ y/D = 0$) to reveal the temporal velocity fluctuations. As shown in Figure 9 at $Re_D = 500$ and $M_\infty = 0.6$, in the 2D simulations, velocity can only fluctuate in the $x$- and $y$-directions. Therefore the appearance of Rossiter modes are two-dimensional phenomena, which are captured in the $u$ and $v$ fluctuations. In the 3D simulations with $W/D = 1$ and 2, the configuration of computational domain allows the flow to fluctuate in the spanwise direction ($z$-direction). However, at this low $Re_D$, the spanwise fluctuation $w'$ appears to be minimal for $W/D = 1$. Once the width is increased to $W/D = 2$, larger fluctuations are observed in the spanwise velocity. In the case W2M06ReLP, although the magnitude of spanwise velocity fluctuation $w'$ is only $5 - 10\%$ of the fluctuation in the $x$- and $y$-direction, it is significant compared to the case with a shorter width of $W/D = 1$. With this addition of spanwise fluctuations, the property of Rossiter modes changes as well. In the spectrum plot of streamwise fluctuation $u'$, Rossiter mode I dominates in the 2D simulation, but the magnitude of Rossiter mode I is reduced by 75% in the case

with $W/D = 2$. Fluctuations in the $y$-direction present a similar trend that flow fluctuates less intensely with increased width of cavity. Even though the dominance of Rossiter mode I is weakened by increasing the width of cavity, Rossiter mode II still remains comparable in magnitude in all these three cases (2D, W1M06ReLP and W2M06ReLP). When the flow is turbulent with $Re_D = 10^4$, the broadband spanwise fluctuations take place regardless of the width of cavity because smaller structures and low viscosity enhance turbulent mixing in all directions. Hence, it suggests that with a low $Re_D$ and wider cavity $W/D = 2$, the velocity fluctuations in the $z$-direction can be observed as well as a reduction of fluctuations in $x$- and $y$-directions. When the flow is turbulent, the effects from the width of cavity on velocity fluctuations in the shear layer are minimal and that fluctuations in all three dimensions are similar in magnitude.

To quantify the overall fluctuations of flow under different configurations, root-mean-square (RMS) of velocity is used to characterize the flow fluctuations. As shown in Figure 10, the distribution of velocity RMS can reveal the region where intense fluctuations take place. In the case of W1M06ReLP, the dominant fluctuations are located in the shear layer as the flow passes the leading edge. The overall fluctuations both in the shear layer and inside the cavity are reduced by extending the width from $W/D = 1$ to 2. The fluctuations in the $z$-direction shown in Figure 9 are also captured in Figure 10 and are primarily observed in the rear part of cavity. These spanwise fluctuations are only observed in the case of a larger width ($W/D = 2$). However, for all spanwise periodic cases with $Re_D = 10^4$, there is no significant difference due to the cavity width. Larger fluctuations are observed near the shear layer with reduced fluctuations inside the cavity, and the magnitudes are comparable in all three directions. In both computational and experimental results, the comparison between periodic- and finite-span cases at $M_\infty = 0.6$ suggests that the fluctuations within the finite-span cavity flow are slightly less intense than those within periodic cavity flows.

Therefore, in the laminar flow, a large width of cavity helps reduce the fluctuations of flow in the $x$- and $y$-directions by introducing small flow variations in the $z$-direction. Due to the viscous flow condition, it requires larger space in the spanwise direction to allow these fluctuations to be triggered. However in the turbulent flow, the chaotic nature of the flow accelerates the development of fluctuations in all directions especially in the spanwise direction, thus the effects from the width of cavity on velocity fluctuations do not strongly depend on the cavity width in the periodic cases. However, in finite-span cavity cases, the existence of no-slip sidewalls leads to reduced velocity fluctuations in the flows.

### D. Spanwise Variation in Flow Field

From the analysis performed above, the cavity width alters the flow field in terms of velocity fluctuations at low $Re_D$. In order to understand the spanwise characteristics of the flow, the averaged velocity $\bar{u}/U_\infty$ from spanwise planes are presented in Figure 11. As seen in Figure 11 at location $x/D = 1$, regardless of $M_\infty$, $Re_D$ and the spanwise boundary conditions, the flow is uniform in the spanwise direction after detaching from the cavity leading edge. Farther downstream at $x/D = 5$, there is observable spanwise variation in the time-averaged streamwise velocity. For the periodic cases, the spanwise variations almost fit one wavelength corresponding to the width of the cavity. In the experiments of full-span cavities at $M_\infty = 0.6$ and 1.4, the ensemble-averaged flows exhibit spanwise variation features at $x/D = 5$ as well. However, these symmetric variations are due to the sidewalls of wind tunnel test section. In the finite-span cavity flow simulations, the variation presents symmetric features are also due to the presence of sidewalls.

With the observation of spanwise variation in the time-averaged flow field, spatial FFT analysis is performed to identify the magnitude of this spanwise variation in the respective flows. Time-averaged data are extracted from a line in the $z$-direction for $(x, y, z)$ with $z \in [z_{\min}, z_{\max}]$ while $x$ and $y$ are held constant. The data are function of spatial coordinates $\bar{f}(x, y, z)$. Spanwise FFT analysis is conducted to obtain the Fourier coefficients $A(x, y, \lambda/W)$ corresponding to $\lambda/W = 1.0, 0.5, 0.25 \ldots$, where $\lambda$ is the spatial wavelength component in the Fourier analysis. The analysis is applied on time-averaged property $\bar{u}/U_\infty$ in the region $0 < x/D < 6$ and $-1 < y/D < 1$ to uncover the coherent spanwise variations inside the cavity. Figure 12 shows the magnitude of Fourier coefficients in a two-dimensional manner. The plots reveals the spanwise variations for a given wavelength $\lambda/W$. Figure 12 only presents spanwise wavelengths of $\lambda/W = 0.25$, 0.5 and 1.0, because the coefficients of shorter wavelengths are negligible compared to these of long wavelengths. This spatial FFT analysis is only performed on the data extracted from the cases with spanwise periodic boundary condition. Because in the finite-span cavity cases, the no-slip sidewalls lead to a large gradient of velocity profile near the sidewall, additional analysis of the flow in the finite-span cavity will be provided in future work. As shown in Figure 12, the spanwise variations are mainly observed in the center and rear regions of the cavity. It is noteworthy that the variations penetrate into the bottom region of the cavity

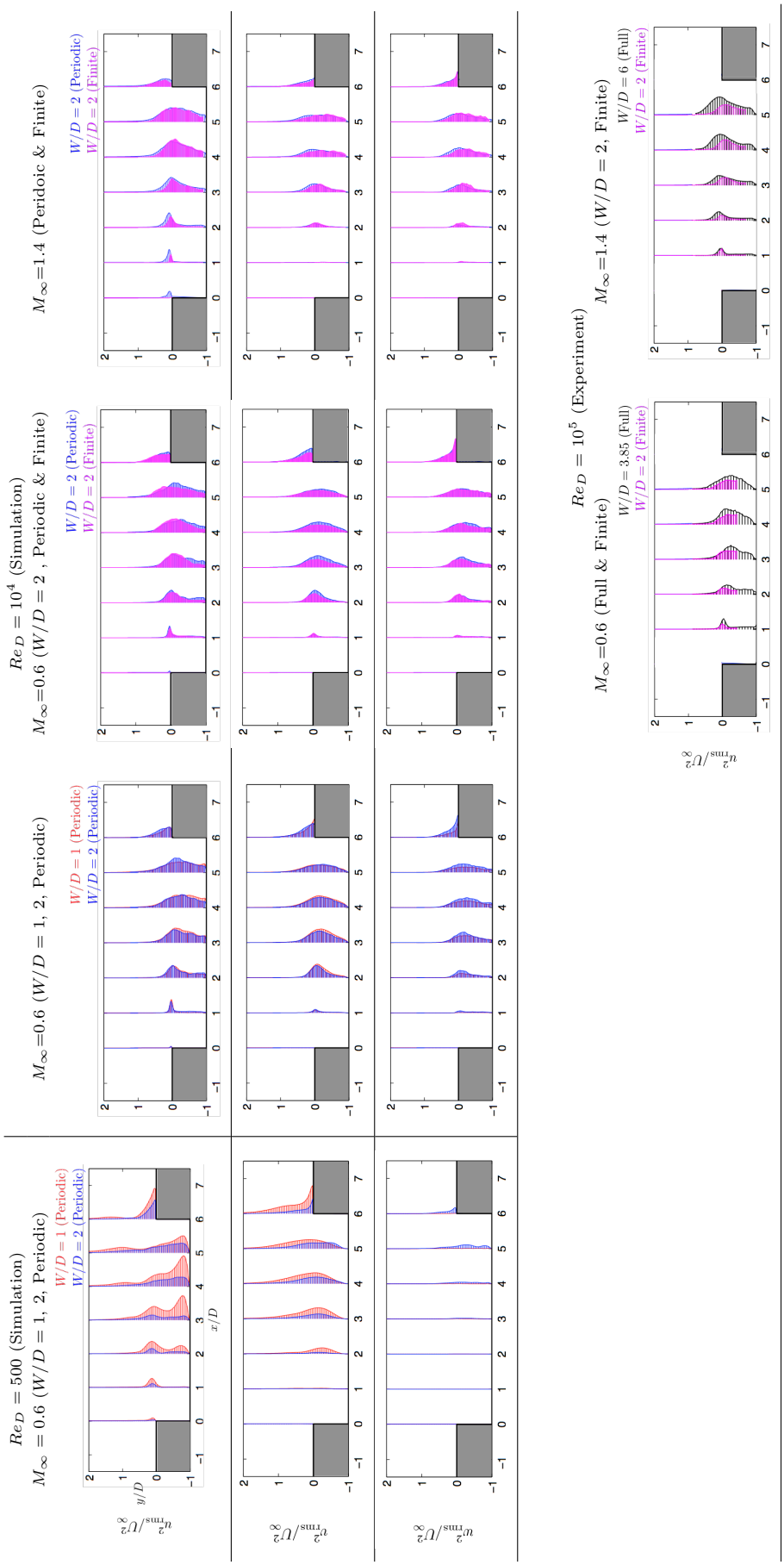


**Figure 10:** Velocity fluctuations $\mathbf{u}^2_{\rm rms}/U^2_\infty$ on center slice ($z/D = 0$) from simulations and experiments. In the simulation results, red: $W/D = 1$ (spanwise periodic); blue: $W/D = 2$ (spanwise periodic); magenta: $W/D = 2$ (finite-span). In the experiment results, black: $W/D = 2$ (full-span); magenta: $W/D = 2$ (finite-span).The magnitudes of $\mathbf{u}^2_{\rm rms}/U^2_\infty$ are scaled by 0.18 for graphical clarity.

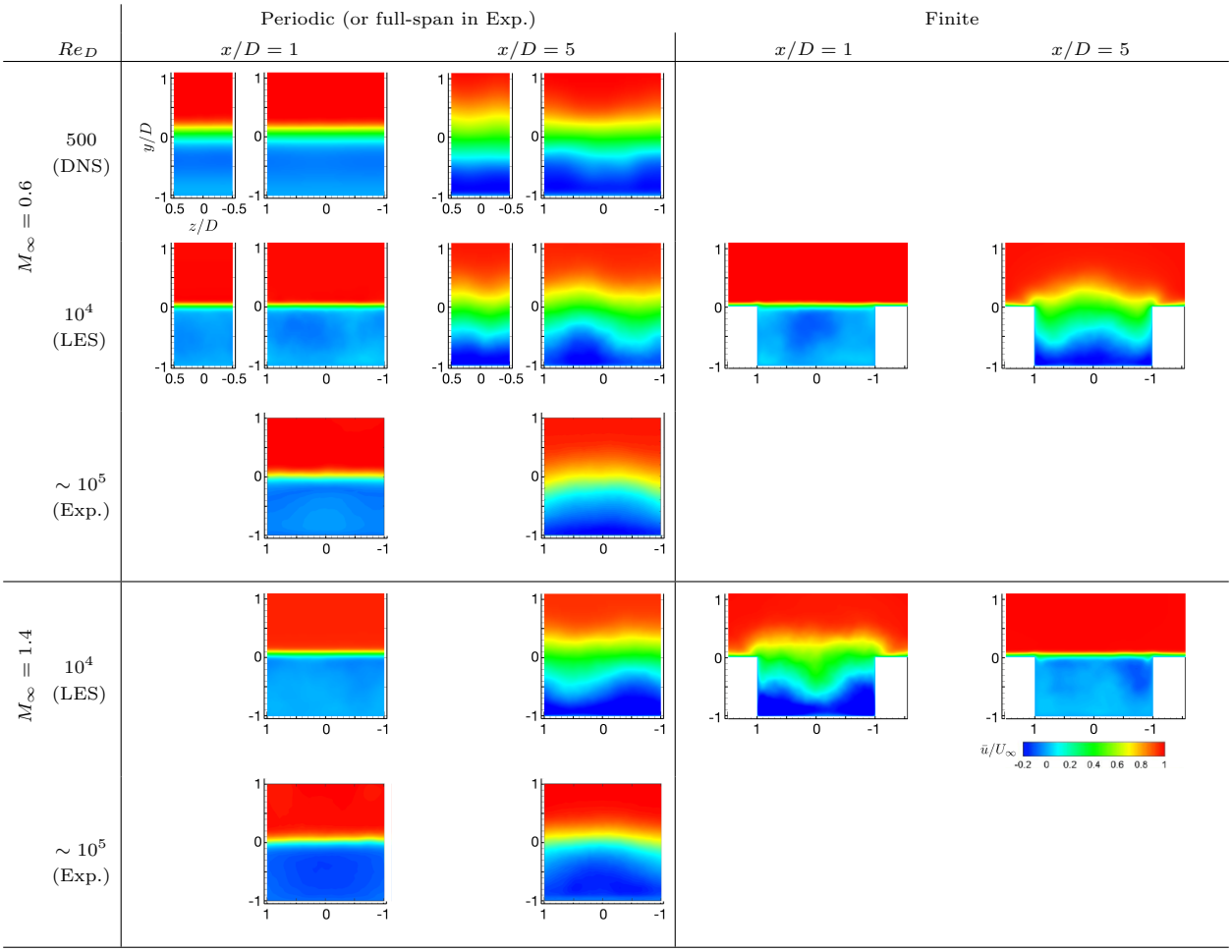


**Figure 11:** Contours of time-averaged streamwise velocity $\bar{u}/U_\infty$ at $x/D$ =1 and 5 from simulations and experiments. Experimental results of full-span cavity at $M_\infty = 1.4$ are reproduced from Lusk's work.[16]

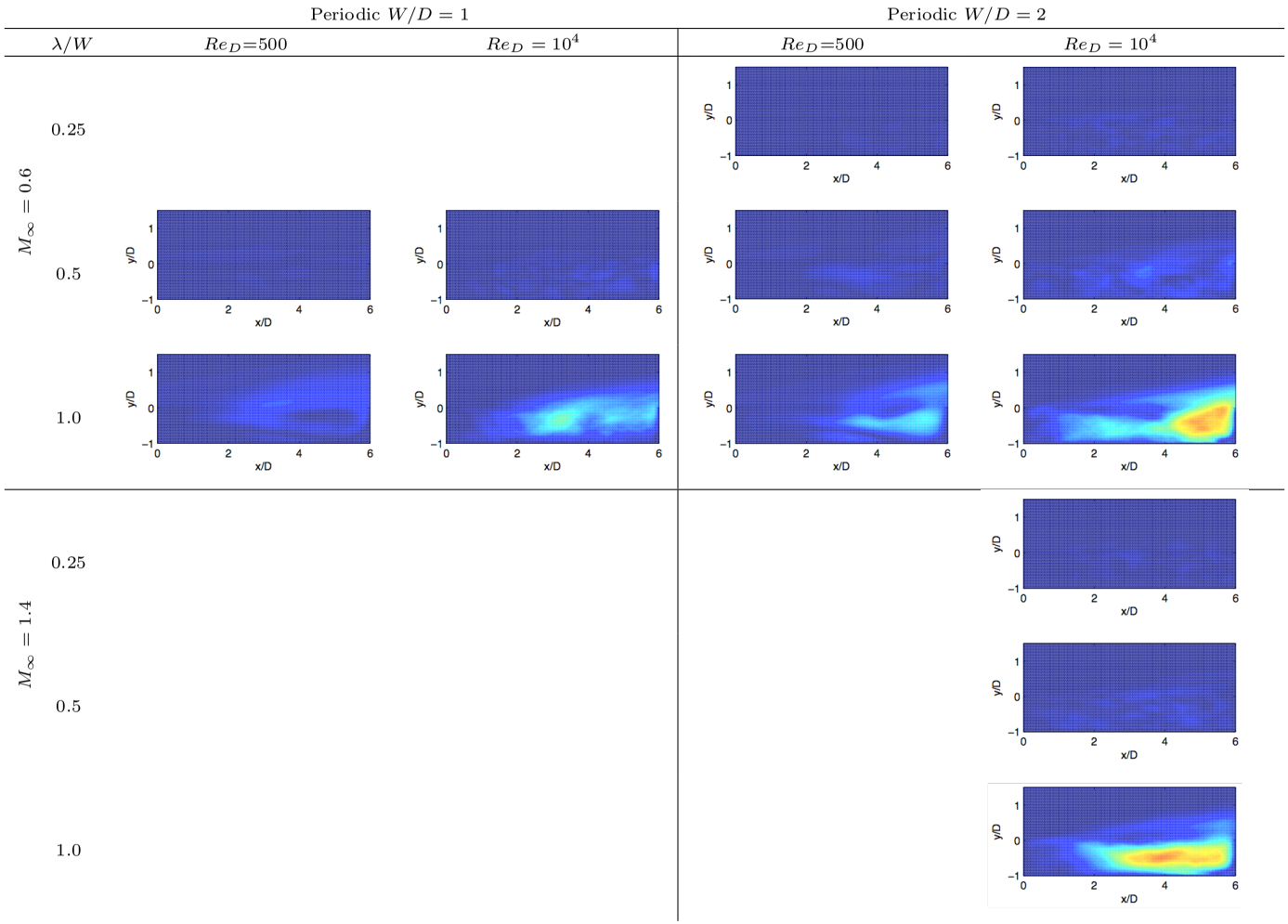


**Figure 12:** Magnitude of spatial Fourier coefficient $A(x,\ y,\ \lambda/W)$ of spanwise variations on time-averaged velocity $\bar{u}/U_\infty$ in the flow field.

as well. With the same cavity geometry and boundary conditions, the spanwise variations are stronger in the flows with high $Re_D$. Furthermore, in all the cases considered, the wavelength of dominant spanwise variation corresponds to the cavity width, but whether it is also true for cavities with wider spanwise extent ($W/D > 2$) still needs additional simulations to gain deeper insights. In the supersonic case, the spanwise variations cover from the center to the rear corner of the cavity and the wavelength of dominant spanwise variation is the cavity width as well, which shares similar features observed in the subsonic flows.

The analyses of spanwise variations are based on 3D nonlinear simulations, which reveal flow unsteadiness in saturated flows. To obtain deeper insights of the effect of cavity width with a spanwise periodic boundary condition, we have companion work on linear global stability to uncover spanwise instabilities of open-cavity flow (not shown here). The spanwise instabilities are analyzed through bi-global stability theory[24] at $Re_D = 500$. The results indicate that there is a secondary instability in the spanwise direction besides the primary instability of Rossiter modes in the open-cavity flows. The spanwise variations exhibited in the simulations of present work stem from 3D modes extracted in the linear global stability analysis, and the linear 3D modes show different growth rates based on the spanwise wavelength.

## IV. Summary

Direct numerical simulations, large eddy simulations, and experiments are performed to study three-dimensional cavity flows for various $M_\infty$, $Re_D$, and spanwise boundary conditions. For the turbulent cases considered, the spanwise coherence of the flow is weakened for wider cavity, especially as the sidewall of finite-span cavity breaks the large spanwise structure into small-scale structures. We assess the spanwise variations in the time-averaged cavity flow and observe the influence of cavity width $W/D$, $M_\infty$ and $Re_D$. The dominant spanwise variation has the same wavelength as the width of cavity in both laminar ($Re_D = 500$) and turbulent ($Re_D = 10^4$) flows. In the subsonic flow at $M_\infty = 0.6$ with $Re_D = 10^4$, the strongest spanwise variation is observed in the rear corner for the spanwise periodic cavity. In the supersonic case at $M_\infty = 1.4$ with $Re_D = 10^4$, large spanwise variations cover a wide region from the center to the rear corner of cavity.

With a low $Re_D$ at $M_\infty = 0.6$, we observed that flow fluctuations are reduced by widening the cavity with periodic boundary conditions. The spanwise configuration allows the flow to develop and fluctuate in the spanwise direction, which reduces the amplitude of Rossiter mode I at a low $Re_D$ condition. As the spanwise variations develop in the flow, the energy from the Rossiter mode is redistributed into the spanwise fluid flow motion. Because the Rossiter mode is a two-dimensional instability, the spanwise motion can extract energy from the primary instability (Rossiter mode) to support the secondary flow with spanwise wavelengths characterized by the depth of cavity. This also explains that the existence of cavity width leads to reduced velocity fluctuations of Rossiter modes. For turbulent flows at $M_\infty = 0.6$ and 1.4, the effects of spanwise boundary condition on the velocity fluctuations in the shear layer are negligible, because the spanwise variations have been established due to high $Re_D$, which do not require a large width to provide space and enable these spanwise variations take place. It has been also noted that in turbulent flows, the finite-span cavity flows have less velocity fluctuations than those with spanwise periodic boundary conditions. In the present study, increasing cavity width and adding sidewalls to the cavity essentially are introducing or triggering spanwise instabilities to the flow, which could lead to redistribution of kinetic energy within the flow. The observations that fluctuations in the flow are altered by the spanwise boundary conditions also implies that there is potential for introducing spanwise variations to suppress the cavity oscillations via flow control techniques. To achieve a better understanding of spanwise instability, linear global stability analysis is underway to uncover the detailed mechanism of spanwise effects in cavity flows.

## Acknowledgments

This research was supported by the U.S. Air Force Office of Scientific Research (Award Number FA9550-13-1-0091, Program Manager: Dr. Douglas Smith). YS and KT thank the support offered by the Research Computing Center at FSU.

## References

[1]Lawson, S. J. and Barakos, G. N., "Review of numerical simulations for high-speed, turbulent cavity flows," *Prog. Aero. Sci.*, Vol. 47, 2011, pp. 186–216.

[2]Rockwell, D. and Naudascher, E., "Self-sustained oscillations of impinging free shear layers," *Annu. Rev. Fluid Mech.*, Vol. 11, 1979, pp. 67–94.

[3]Cattafesta, L. N., Song, Q., Williams, D. R., Rowley, C. W., and Alvi, F. S., "Active control of flow-induced cavity oscillations," *Prog. Aero. Sci.*, Vol. 44, 2008, pp. 479–502.

[4]Colonius, T., Basu, A. J., and Rowley, C. W., "Numerical investigation of the flow past a cavity," AIAA Paper 1999-1912, 1999.

[5]Arunajatesan, S., Barone, M. F., Wagner, J. L., Casper, K. M., and Beresh, S. J., "Joint experimental/computational inversigation into the effects of finite width on transonic cavity flow," AIAA Paper 2014-3027, 2014.

[6]Beresh, S. J., Wagner, J. L., Pruett, B. O. M., and Henfling, J. F., "Supersonic flow over a finite-width rectangular cavity," *AIAA J.*, Vol. 53, No. 2, 2015.

[7]Sun, Y., Nair, A. G., Taira, K., Cattafesta, L. N., Bres, G. A., and Ukeiley, L. S., "Numerical simulations of subsonic and transonic open-cavity flows," AIAA Paper 2014-3092, 2014.

[8]Brès, G. A. and Colonius, T., "Three-dimensional instabilities in compressible flow over open cavities," *J. Fluid Mech.*, Vol. 599, 2008, pp. 309–339.

[9]d. Vicente, J., Basley, J., Garrido, F. M., Soria, J., and Theofilis, V., "Three-dimensional instabilities over a rectangular open cavity: from linear stability analysis to experimentation," *J. Fluid Mech.*, Vol. 748, No. 189-220, 2014.

[10]Brès, G. A., Nichols, J. W., Lele, S. K., , and Ham, F. E., "Towards best practices for jet noise predictions with unstructured large eddy simulations," AIAA Paper 2012-2965, New Orleans, 2012.

[11]Vreman, A. W., "An eddy-viscosity subgrid-scale model for turbulent shear flow: algebraic theory and applications," *Phys. Fluids*, Vol. 16, No. 10, 2004, pp. 3670–3681.

[12]Toro, E. F., Spruce, M., and Speares, W., "Restoration of the contact surface in the HLL-Riemann solver," *Shock Waves*, Vol. 4, 1994, pp. 25–34.

[13]Béchara, W., Bailly, C., Lafon, P., and Candel, S. M., "Stochastic approach to noise modeling for free turbulent flows," *AIAA J.*, Vol. 32, No. 3, 1994, pp. 455–463.

[14]Franck, J. A. and Colonius, T., "Compressible large eddy simulation of separation control on a wall-mounted hump," *AIAA J.*, Vol. 48, No. 6, 2010, pp. 1098–1107.

[15]Freund, J. B., "Proposed inflow/outflow boundary condition for direct computation of aerodynamic sound," *AIAA J.*, Vol. 35, No. 4, 1997, pp. 740–742.

[16]Lusk, W. T., Cattafesta, L. N., and Ukeiley, L. S., "Leading edge slot blowing on an open cavity in supersonic flow," *Exp Fluids*, Vol. 53, 2012, pp. 187–199.

[17]Zhang, Y., Sun, Y., Arora, N., Cattafesta, L., Taira, K., and Ukeiley, L., "Suppression of cavity oscillations via three-dimensional steady blowing," AIAA Paper 2015-3219, 2015.

[18]Beresh, S. J., Wagner, J. L., and Pruett, B. O. M., "Particle image velocimetry of a three-dimensional supersonic cavity flow," AIAA Paper 2012-30, 2012.

[19]George, B., Ukeiley, L., Cattafesta, L., and Taira, K., "Control of three-dimensional cavity flow using leading-edge slot blowing," AIAA 2015-1059, 2015.

[20]Hunt, J. C. R., Wray, A. A., and Moin, P., "Eddies, streams, and convergence zones in turbulent flows," *Proc. of the Summer Program, Center of Turbulence Research*, 1988, pp. 193–208.

[21]Rowley, C. W., Colonius, T., and Basu, A. J., "On self-sustained oscillations in two-dimensional compressible flow over rectangular cavities," *J. Fluid Mech.*, Vol. 455, 2002, pp. 315–346.

[22]Murray, N., Sällström, E., and Ukeiley, L., "Properties of subsonic open cavity flow fields," *Phys. Fluids*, Vol. 21, 2009.

[23]Rowley, C. W., *Modeling, simulation, and control of cavity flow oscillations*, Ph.D. thesis, California Institute of Technology, August 2001.

[24]Theofilis, V., "Advances in global linear instability analysis of nonparallel and three-dimensional flows," *Prog. Aero. Sci.*, Vol. 39, 2003, pp. 249–315.